

Hydrodynamics of Taylor flow in noncircular capillaries

Dingsheng Liu^{a,b}, Shudong Wang^{a,*}

^a Dalian Institute of Chemical Physics, Chinese Academy of Sciences, Dalian 116023, China

^b Graduate School of Chinese Academy of Sciences, Beijing 100039, China

Received 1 March 2007; received in revised form 21 October 2007; accepted 28 October 2007

Available online 17 November 2007

Abstract

In this work, volume of fluid (VOF) technique, one computational fluid dynamics (CFD) method, was used to investigate the upward Taylor flow in vertical square and equi-triangular capillaries. For saving computation time, the simulations were carried out in a moving frame of reference attached to Taylor bubbles. The main flow parameters, involving bubble size and shape, liquid film thickness, velocity field and two-phase relative velocity, were studied as functions of capillary number. The numerical simulations were in good agreement with previous reports and showed that the flow in the sides and corners of polygonal capillaries were different. A comparative study was also conducted on Taylor flow in square and equi-triangular capillaries and their circular counterparts, where the influence of capillary geometry on the characteristics of Taylor flow was illustrated clearly.

© 2007 Elsevier B.V. All rights reserved.

Keywords: Taylor flow; VOF; Square capillary; Equi-triangular capillary; Monolithic reactor

1. Introduction

Gas–liquid–solid monolithic reactors are attracting considerable attention from laboratory to chemical industry [1–5]. In comparison with conventional trickle bed and slurry reactors, monolithic reactors have several advantages, such as high mass transfer rate, low-pressure drop and ease of scale up [1–5]. Generally, a monolith consists of uniformly parallel channels with circular, square, triangular or other cross sections, which have dimensions typically in the range of 1–5 mm. Provided gas and liquid phases were distributed uniformly in the various channels of the monolith, the information obtained from a single channel can, in principle, be employed to scale up commercial reactors [3,4]. Therefore, the hydrodynamics occurring in a single channel is an important research field.

Taylor flow in a single capillary or channel has been extensively investigated because the flow pattern is very common and important in gas–liquid–solid monolithic reactors. Taylor flow consists of trains of long bubbles separated by liquid slugs flowing concurrently inside a capillary. The gas-to-wall mass transfer is increased remarkably due to the existence of thin liquid film

between the bubbles and capillary walls. A recirculation pattern is induced in the liquid slug trapped between two consecutive bubbles, which enhances the radial mass transfer greatly and makes solution concentration more uniform. At the same time, the axial segregation of the bulk liquid significantly reduces the axial dispersion of the solute [6,7]. In a capillary, Taylor flow is essentially laminar, liquid slugs are free of small gas bubbles, and the coalescence and breakage of the bubbles are virtually absent.

Dated back to 1935, Fairbrother et al. [8] pointed out that, for the motion of a long bubble in liquid flowing in a capillary, gas bubble velocity, U_b , and liquid slug velocity, U_L , were directly related. The relation could be expressed as an empirical correlation: $W = (U_b - U_L)/U_b = 1.0Ca^{1/2}$, $7.5 \times 10^{-5} < Ca < 10^{-2}$, $Ca = \mu_L U_b / \sigma$, where Ca is the capillary number, is the ratio of the viscous force to the capillary force, μ_L and σ denote the liquid molecular viscosity and gas–liquid surface tension, respectively. In 1960, Taylor [9] extended the above result up to $Ca = 0.1$, and found that W approached an asymptotic limit of 0.56 at $Ca = 2.0$. Bretherton [10] used lubrication approximation to analyze the relationship between W and Ca , and presented $W = 1.29(3Ca)^{2/3}$, from which the result obtained was in error by no more than 10% for $Ca < 0.005$. Thulasidas et al. [11] calculated W in circular and square capillaries in the range of $10^{-3} < Ca < 3$. The work showed that the limit value of W approached 0.58 in circular capillaries and 0.6 in square capillaries. The relationship

* Corresponding author. Tel.: +86 411 84662365; fax: +86 411 84662365.
E-mail address: Wangsd@dicp.ac.cn (S. Wang).

between W and Ca was also studied based on CFD simulation by Taha et al. [12], recently.

Liquid film thickness is an important parameter for Taylor flow in capillaries. Using a photocell, Irandoost et al. [13] measured the liquid film thickness for air–water, air–ethanol and air–glycerol systems and proposed the empirical formula $\delta/d = 0.18\{1 - \exp[-3.1(\mu_L U_b/\sigma)^{0.54}]\}$, where δ is the liquid film thickness and d is the capillary diameter. Thulasidas et al. [11] studied the dimensionless liquid film thickness for $0.004 < Ca < 3$ in circular and square capillaries by a CCD camera. Adopting Taylor's experimental data [9], Aussillous et al. [14] fitted a semi-empirical correlation $\delta/d = 0.66Ca^{2/3}/(1 + 3.33Ca^{2/3})$.

Taylor [9] pioneered to give a rough sketch describing the streamline patterns in the liquids in the front of the bubbles. The sketch showed that a complete bypass flow occurred at $W > 0.5$, and two different toroidal vortex flow appeared at $W < 0.5$. Thulasidas et al. [15] used a particle imaging velocimetry to elucidate the details of the flow structure and also observed the complete bypass flow and vortex flow in the liquid slugs in the frame of reference attached to the bubbles.

In comparison with circular capillaries, Taylor flow inside polygonal capillaries has not been studied until recently for its practical importance. Taylor flow through square capillaries has many interesting analogies with two-phase flow in porous media. For instance, in oil recovery the wetting film thickness is a direct measure of the fraction of oil which cannot be recovered. Square capillaries provide a better model for describing the irregular and angular nature of porous media than that obtained from circular capillaries. More recently, the optimum design and operation of three-phase monolithic reactors requires more comprehensive understanding of the characteristics of Taylor flow in square channels. Therefore, researchers have conducted experimental and theoretical studies on Taylor flow in square capillaries [11,15–22]. These researches were concerned with the bubble shape, liquid film thickness, velocity fields in the liquids, wall shear forces and so on.

Despite that monoliths with triangular channels are currently applied in some areas [23], the detailed hydrodynamics characteristics in triangular channels have received much less attention. Wilson et al. [24] and Groppi et al. [25] investigated the heat and mass transfer of the gas phase in triangular channels. Moreover, triangular channels have a strong similarity with sinusoidal ones, i.e. the typical channels in metallic monoliths. To our knowledge, few studies on Taylor flow in triangular channels were reported until now.

Since 1990s, CFD has become a powerful tool for revealing the mechanism of Taylor flow. The VOF method proposed by Hirt et al. [26] is a popular and effective tool for simulating Taylor flow. The VOF model can simulate two immiscible fluids by solving a single set of momentum equations and tracking the volume fraction of each phase throughout the computational domain [26,27]. The feasibility of the VOF method in direct simulation of Taylor flow was confirmed by the pioneering work of Tomiyama et al. [28,29].

In the present work, the VOF technique similar to Taha et al. [12] was used to simulate the upward Taylor flow in vertical

square and equi-triangular capillaries. Three orders of magnitude changes of Ca , 0.003–1, were covered here and the inertial effects were included. During the simulations, the densities of liquid and gas were 998.2 and 1.225 kg/m³, respectively. The gas–liquid surface tensions used were 0.072 N/m for $Ca \leq 0.09$ and 0.0072 N/m for $Ca \geq 0.1$. The gas bubble velocities were a constant value, 0.5 m/s. The main parameters, including bubble shape and size, liquid film thickness, flow field and two-phase relative velocity, were investigated. The simulations were compared with previous studies.

2. Theoretical and numerical methodology

2.1. Governing equations

The continuum and momentum equations for incompressible, gas–liquid two-phase flow throughout the computational domain are given by the following expressions:

$$\frac{\partial \rho}{\partial t} + \nabla \cdot (\rho \vec{v}) = 0 \quad (1)$$

$$\frac{\partial(\rho \vec{v})}{\partial t} + \nabla \cdot (\rho \vec{v} \vec{v}) = -\nabla p + \nabla \cdot [\mu(\nabla \vec{v} + \nabla \vec{v}^T)] + \rho \vec{g} + \vec{F} \quad (2)$$

The equations above are related with the volume fractions of gas and liquid phases through the density, ρ , and viscosity, μ . The properties appearing in the transport equations are determined by the presence of the component phases in each control volume. Thus the properties in any given grid cell are either purely representative of one of the phases, or representative of a mixture of the phases, depending upon the volume fraction value, α . If the gas and liquid phases are denoted as the subscripts G and L, respectively, the density and viscosity in each cell are given by

$$\rho = \alpha_L \rho_L + (1 - \alpha_L) \rho_G \quad (3)$$

$$\mu = \alpha_L \mu_L + (1 - \alpha_L) \mu_G \quad (4)$$

In the VOF model, the following three conditions are possible for the liquid phase volume fraction α_L in a given cell. (1) $\alpha_L = 0$: the cell is empty of the liquid phase; (2) $\alpha_L = 1$: the cell is full of the liquid phase; (3) $0 < \alpha_L < 1$: the cell contains the gas–liquid interface [26,27]. The tracking of the gas–liquid interface is accomplished by solving a continuity equation for the liquid phase volume fraction, α_L [27]:

$$\frac{\partial \alpha_L}{\partial t} + \vec{v} \cdot \nabla \alpha_L = 0 \quad (5)$$

The gas phase volume fraction will be computed based on the following constraint:

$$\alpha_G + \alpha_L = 1 \quad (6)$$

Gas–liquid surface tension is very important in Taylor flow. The surface tension model applied here is the continuum surface force (CSF) model proposed by Brackbill et al. [30]. With this model, the addition of surface tension to the VOF calculation

results in a source term of the momentum equation. The source term has the following form for the gas–liquid phases:

$$\vec{F} = \sigma \frac{\rho_{KL} \nabla \alpha_L}{(1/2)(\rho_G + \rho_L)} \quad (7)$$

where σ is the gas–liquid surface tension coefficient. The curvature, κ_L , is defined in terms of the divergence of the unit normal, \hat{n} :

$$\kappa_L = \nabla \cdot \hat{n} = \frac{1}{|\vec{n}|} \left[\left(\frac{\vec{n}}{|\vec{n}|} \cdot \nabla \right) |\vec{n}| - (\nabla \cdot \vec{n}) \right] \quad (8)$$

where

$$\hat{n} = \frac{\vec{n}}{|\vec{n}|}, \quad \vec{n} = \nabla \alpha_L \quad (9)$$

2.2. Model geometries and boundary conditions

Taylor flow in square and equi-triangular capillaries with the same hydraulic diameters of 1 mm was simulated. As illustrated in Figs. 1 and 2, 3-D Cartesian coordinate systems were used and the computational domains were 1/8 prism for square capillaries and 1/6 prism for equi-triangular capillaries. The shadow regions ABC in Fig. 1 represented the cross sections of the computational domains. The symbols \otimes implied that Z-direction was opposite to the reader and vertical to the paper. The coordinate systems and computational domains adopted saved computation time greatly, while no useful information was lost.

The length of the computational domains was 16 times of the capillary hydraulic diameters. The model geometries and boundary conditions were given in Fig. 2. A velocity inlet boundary condition was used to set a fully developed velocity profile at the inlet by a user defined function (UDF). Outflow and no-slip boundary conditions were provided at the outlet and wall (BC plane), respectively. On the AC and AB planes, the symmetry boundary conditions were adopted, not displayed in Fig. 2.

2.3. Simulation scheme

The simulations were carried out in a unit cell of Taylor flow as shown in Fig. 2. A bubble, made up of a cylinder and two hemispheres at its two ends, was patched in the center of the

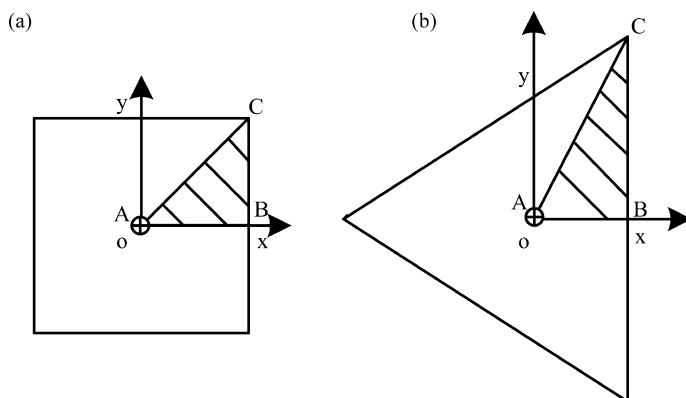


Fig. 1. The cross sections (shadow regions) of computational domains in capillaries: (a) square capillaries; (b) equi-triangular capillaries.

Velocity-inlet (set by UDFs)

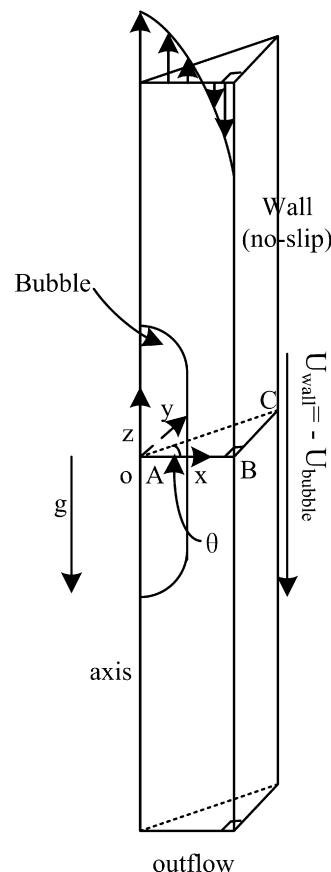


Fig. 2. Computational domains and boundary conditions applied on them: $\theta = 45^\circ$ for square capillaries; $\theta = 60^\circ$ for equi-triangular capillaries.

domains at the beginning of each simulation. Only the parts of the bubbles inside the shaded areas in Fig. 1 were simulated. In fact, the simulations confirmed that the initial shape of the bubble only affected the time of computation convergence, but did not influence the bubble's final shape. The shape and volume

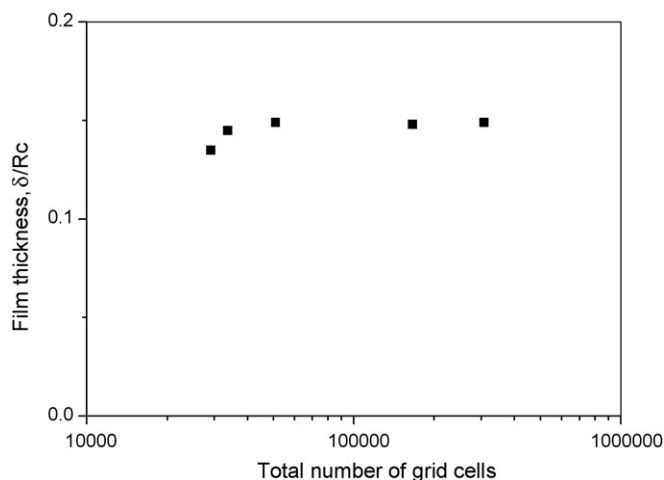


Fig. 3. The effect of the number of grid cells on liquid film thickness on the side plane (AB direction) of a square capillary for $Ca = 0.3$; $\rho_L = 998.2 \text{ kg/m}^3$; $U_b = 0.5 \text{ m/s}$; $\sigma = 0.0072 \text{ N/m}$; $d = 0.001 \text{ m}$.

of the initial bubbles adopted were the same in square and equi-triangular capillaries. The frame of reference used was attached to the bubbles. Thus, the bubble was stationary and the capillary wall moved down with the rising velocity of the bubble.

The computational domains were discretized with GAMBIT mesh generation software, using hexahedral cells. Finer meshes were used near the gas–liquid interface, the wall and symmetry plane in order to get higher numerical precision. Confidence of grid independence results was gained by increasing the number of grid cells for a few representative simulations. For example, the effect of the number of grid cells on the liquid film thickness was illustrated in Fig. 3. The liquid inlet velocity function was iteratively adjusted until the position and shape of the bubble were stable in the domain at the end of each simulation. The Courant number was 0.25. The time step was 10^{-8} – 10^{-4} second according to different grid sizes and liquid inlet velocities. The shorter the time step was, the longer the computational time was. The geometric reconstruction scheme based on the piecewise-linear approach originated by Youngs [31] was used to reconstruct the bubble free surface. The computational domains with $\alpha_L = 0.5$ were considered to represent the gas–liquid interface. The simulations were realized by using Fluent CFD software package.

3. Numerical simulation results and discussions

3.1. Bubble shape

Figs. 4–6 showed the profiles of the Taylor bubbles, as a function of Ca , in square and equi-triangular capillaries. Different from circular capillaries, the Taylor bubbles in square and equi-triangular capillaries were not circular symmetric at low and intermediate Ca , and flattened out against the walls leaving accumulative liquids in the corners. The momentum transfer from the corners to the liquids was larger than that from the sides of the polygonal capillaries. Thus, liquid flowed more slowly in the corners and the pressure field was shaped by

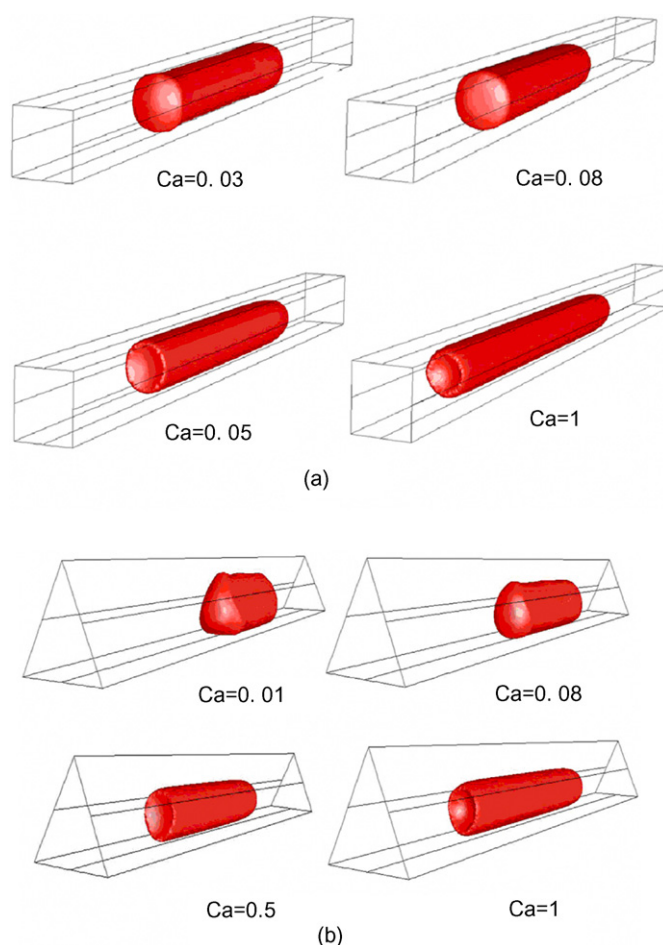


Fig. 4. Taylor bubbles upflowing in vertical polygonal capillaries: (a) square capillaries; (b) equi-triangular capillaries; $\rho_L = 998.2 \text{ kg/m}^3$; $U_b = 0.5 \text{ m/s}$; $d = 0.001 \text{ m}$; $\sigma = 0.072 \text{ N/m}$ for $Ca = 0.01, 0.03$ and 0.08 ; $\sigma = 0.0072 \text{ N/m}$ for $Ca = 0.5$ and 1 .

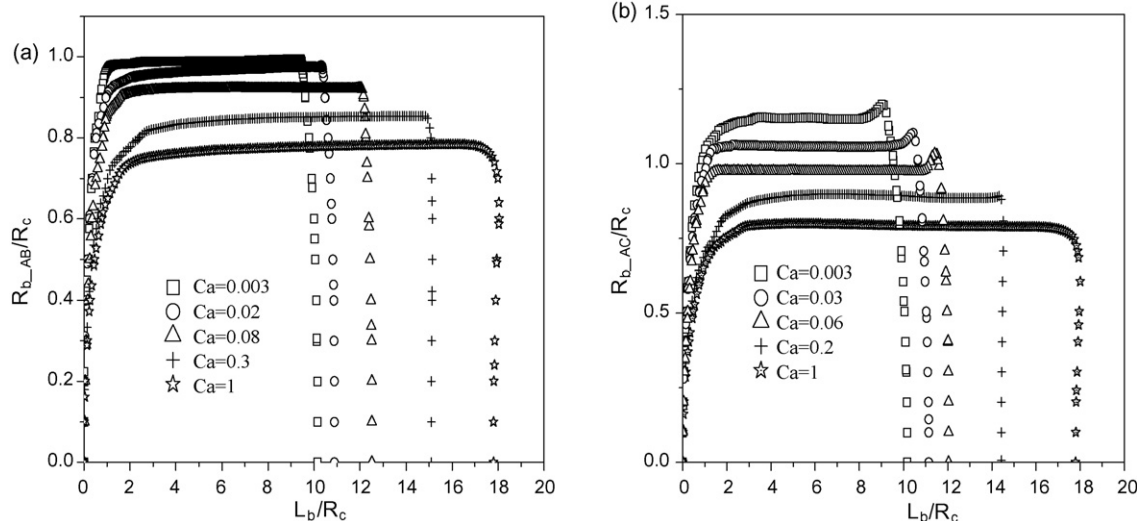


Fig. 5. The profiles of the Taylor bubbles in square capillaries: (a) AB direction; (b) AC direction; $\rho_L = 998.2 \text{ kg/m}^3$; $U_b = 0.5 \text{ m/s}$; $d = 0.001 \text{ m}$; $\sigma = 0.072 \text{ N/m}$ for $Ca = 0.003, 0.02, 0.03, 0.06$ and 0.08 ; $\sigma = 0.0072 \text{ N/m}$ for $Ca = 0.2, 0.3$ and 1 .

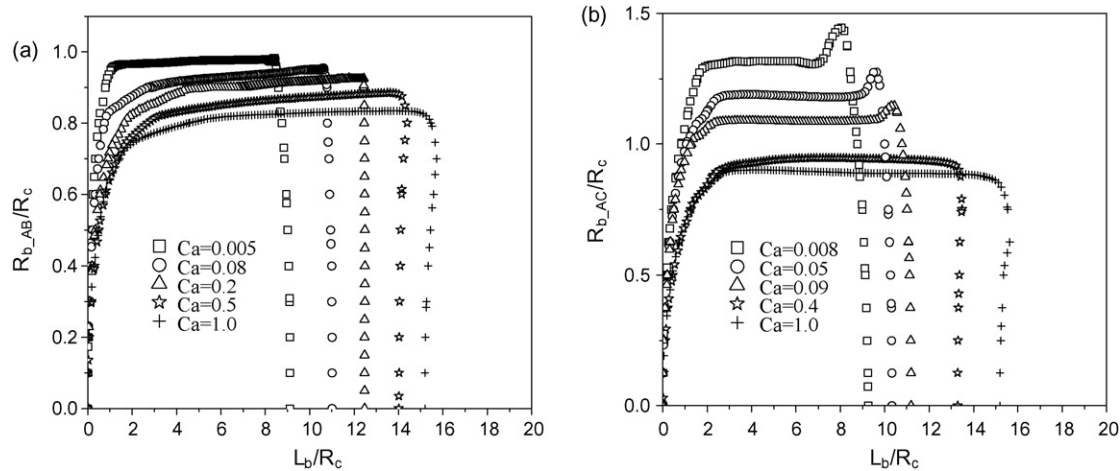


Fig. 6. The profiles of Taylor bubbles in equi-triangular capillaries: (a) AB direction; (b) AC direction; $\rho_L = 998.2 \text{ kg/m}^3$; $U_b = 0.5 \text{ m/s}$; $d = 0.001 \text{ m}$; $\sigma = 0.072 \text{ N/m}$ for $Ca = 0.005, 0.008, 0.05, 0.08$ and 0.09 ; $\sigma = 0.0072 \text{ N/m}$ for $Ca = 0.2, 0.4, 0.5$ and 1.0 .

the contribution of the viscous force, inertial force and surface tension. Similar phenomena have also been observed by other researchers [16,20]. Figs. 4–6 showed that the bubble profiles transformed non-circular into circular symmetry gradually with Ca increasing. The gas–liquid surface, defined by a dimensionless bubble radius R_b/R_c , was plotted against Ca with respect to diagonal plane (AC direction) and side plane (AB direction) in Figs. 5 and 6, where R_b was the bubble radius, measured at the midpoint of the bubble in AB or AC direction, and R_c was the capillary hydraulic radius. The bubbles were not circular symmetric at low Ca , which was shown by the difference of R_b/R_c in AB and AC directions. With Ca increasing, the bubble radius decreased simultaneously in AB and AC directions in Fig. 7. The decrease rate of the bubble radius in AC direction was faster than that in AB direction. Fig. 7a showed that the bubble radius in AC direction gradually decreased, and overlapped with that in AB direction at $Ca = 0.1$ in square capillaries. The data was consistent with that measured by Kolb et al. [16] in their experiment, but larger than the numerical result, $Ca = 0.04$, calculated by Hazel et al. [22]. The difference might arise from the following two causes. First, inertial effect was included in our study, while

not by Hazel et al. Second, a finitely long bubble was simulated here and the radius at the midpoint of the bubble was considered, while a “bubble” with the back-end-open was studied and the radius was measured at 11 half-widths behind the bubble tip by Hazel et al. Fig. 7b showed that, in equi-triangular capillaries, the bubble radius in diagonal and side planes did not decreased to the same value in our simulations. However, from the trend of the decreasing, it could be concluded that the bubble radius in AB and AC directions would also be same at a large Ca .

Figs. 4–6 showed that the profile of a Taylor bubble was not uniform along the axis of the bubble. The bubble consisted of five distinct regions: the nose, the rear, the uniform film region in the middle of the bubble, as well as the front transition region connecting the nose and the uniform film, and the back transition region connecting the rear and the uniform film [10,12]. While Ca increased, the thickness of liquid film and the sharpness of bubble nose increased, and the rear of the bubble transformed a convexity into a concave. The transition regions were also extended. The influence of Ca on the rear of the bubble was greater than the nose of the bubble. The wave disturbance could be observed at the rear of the bubble at low Ca , while with Ca

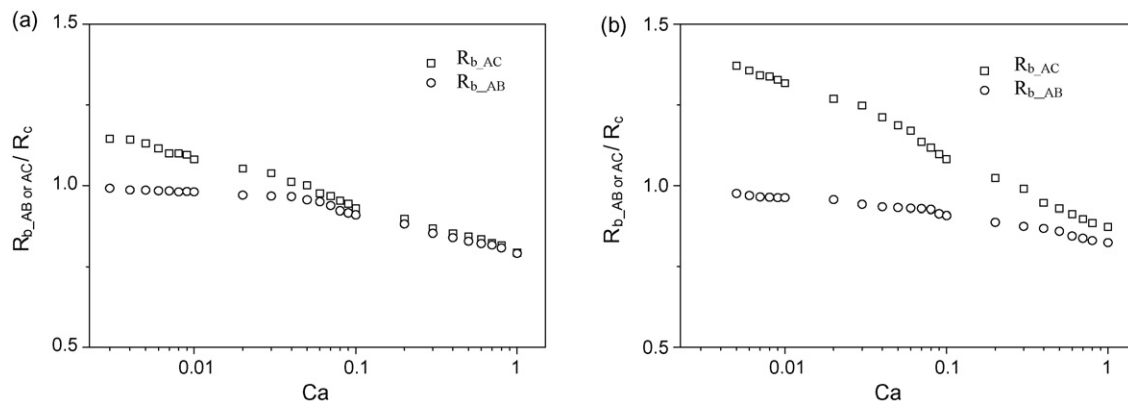


Fig. 7. Transition in Taylor bubble symmetry: (a) square capillaries; (b) equi-triangular capillaries; $\rho_L = 998.2 \text{ kg/m}^3$; $U_b = 0.5 \text{ m/s}$; $d = 0.001 \text{ m}$; $\sigma = 0.072 \text{ N/m}$ for $Ca \leq 0.09$; $\sigma = 0.0072 \text{ N/m}$ for $Ca \geq 0.1$.

increasing it became slight and even disappeared finally, which was also noticed by the previous researchers [12,32].

3.2. Film thickness

As shown in Fig. 7, with decreasing Ca , the liquid film in the side plane (unless otherwise mentioned) became thinner. The influences of capillary geometry on the liquid film thickness were displayed in Fig. 8. The numerical results obtained from the Taylor flow in square capillaries were compared with the reports published by Thulasidas et al. [11], Kolb et al. [16], and Hazel et al. [22]. The same trend of the liquid film was found, but our numerical results were smaller at larger Ca . Fig. 8 also showed the simulations in equi-triangular capillaries. To our knowledge, few studies were reported for Taylor flow in equi-triangular capillaries. As mentioned previously, in square and equi-triangular capillaries, the capillary hydraulic diameters and the volume of the initial Taylor bubbles were the same. The liquid film thickness in circular capillaries was larger than that in square and equi-triangular capillaries in the whole range of Ca . The reason was that the symmetry of a circular capillary led to a uniform liquid film between Taylor bubbles and the walls. However, in square and equi-triangular capillaries, most of the liquid was squeezed into the corners by the transformed bubbles, which resulted in thinner liquid films on side planes.

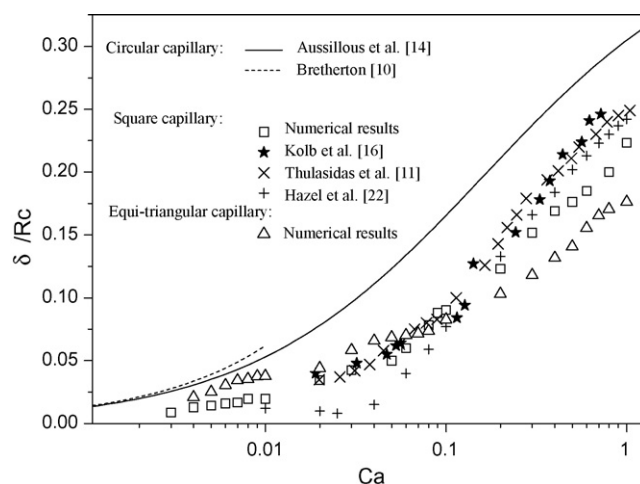


Fig. 8. Dimensionless film thickness, as a function of Ca on side planes. Parameters used in the simulations: $\rho_L = 998.2 \text{ kg/m}^3$; $U_b = 0.5 \text{ m/s}$; $d = 0.001 \text{ m}$; $\sigma = 0.072 \text{ N/m}$ for $Ca \leq 0.09$; $\sigma = 0.0072 \text{ N/m}$ for $Ca \geq 0.1$.

3.3. Velocity fields in liquid slugs

Figs. 9 and 10 showed the velocity fields around Taylor bubbles rising in square and equi-triangular capillaries. Note that the frames of reference were attached to the Taylor bubbles.

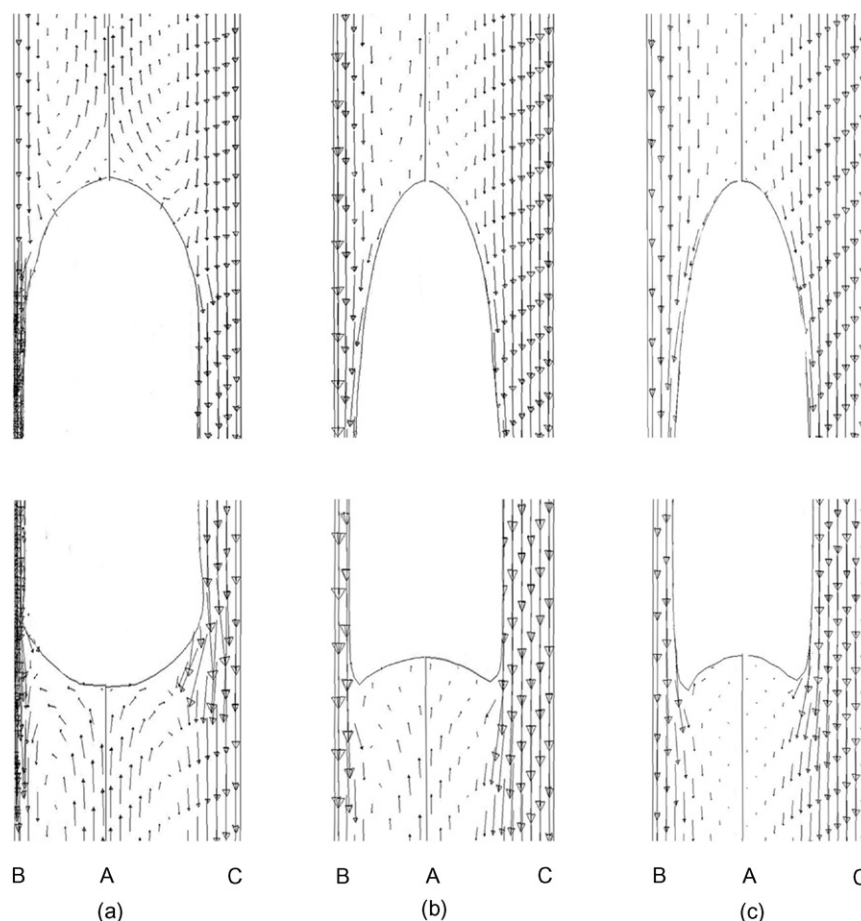


Fig. 9. Liquid velocity fields around Taylor bubbles in vertical square capillaries: (a) $Ca = 0.08$, (b) $Ca = 0.5$ and (c) $Ca = 1.0$; $\rho_L = 998.2 \text{ kg/m}^3$; $U_b = 0.5 \text{ m/s}$; $d = 0.001 \text{ m}$; $\sigma = 0.072 \text{ N/m}$ for $Ca = 0.08$; $\sigma = 0.0072 \text{ N/m}$ for $Ca = 0.5$ and 1.0 .

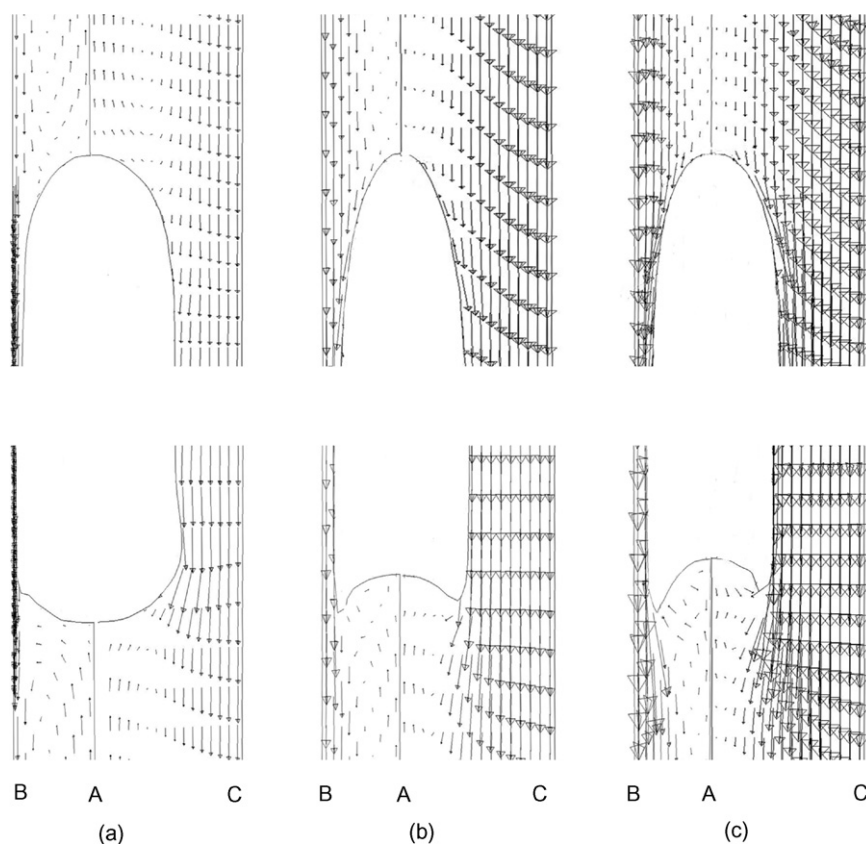


Fig. 10. Liquid velocity fields around Taylor bubbles in vertical equi-triangular capillaries: (a) $Ca = 0.08$, (b) $Ca = 0.6$ and (c) $Ca = 1.0$; $\rho_L = 998.2 \text{ kg/m}^3$; $U_b = 0.5 \text{ m/s}$; $d = 0.001 \text{ m}$; $\sigma = 0.072 \text{ N/m}$ for $Ca = 0.08$; $\sigma = 0.0072 \text{ N/m}$ for $Ca = 0.6$ and 1.0 .

Thus, the velocity fields were relative to the bubbles. At low and intermediate Ca , the liquid ahead of a bubble flowed downward and divided into two streams near the bubble nose. One went on flowing downward and formed a thin liquid film, separating the bubble from the capillary wall. While the other retraced upward, flowed away from the bubble and formed a toroidal vortex before the bubble nose. Figs. 11 and 12 showed that the distribution of the vortex centers also approximated to squares and equi-triangles, respectively, owing to the non-circular-symmetric characteristics of the flow. With increasing Ca , the distribution transformed a square or equi-triangle into a circle gradually. The propagation of the vortex centers was consistent with that of Taylor bubble cross sections. The toroidal vortex, also termed a stagnation ring, moved at the same velocity as that of the bubble. Thus, it was stationary relative to the bubble. The center of the toroidal vortex gradually shifted toward the centerline of the capillary with increasing Ca , so that the more liquid flowed toward the bubble and formed a thicker liquid film. Upon further increasing Ca , the radius of the stagnation ring would decrease and even disappear at the critical Ca , at which the bubble velocity equaled to the maximum liquid velocity [16]. And only the fluid on the axis of the capillary was stationary and the toroidal vortex vanished completely. The critical Ca , obtained in our simulation, was 0.8 and 1.0 in square and equi-triangular capillaries, respectively. The value 0.8 in square capillaries was close to the value 0.65 measured by Kolb et al. [16]. If Ca further increased, all the liquid would flow downward and form the liquid film, which

was called complete bypass flow. As illustrated in Figs. 9 and 10, the liquid below the rear of the bubble also formed a stagnation ring. Contrary to the conditions at the bubble nose, the liquid outside the ring flowed away from the bubble while the liq-

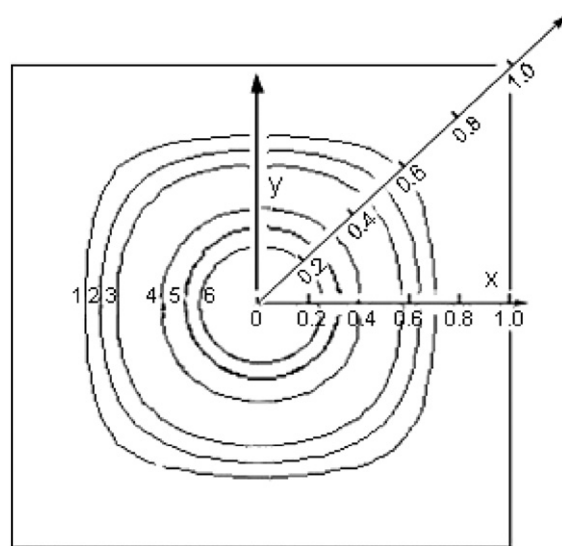


Fig. 11. Toroidal vertices distribution across a square capillary d before the bubble nose: (1) $Ca = 0.008$, (2) $Ca = 0.03$, (3) $Ca = 0.08$, (4) $Ca = 0.5$, (5) $Ca = 0.7$ and (6) $Ca = 0.8$; $\rho_L = 998.2 \text{ kg/m}^3$; $U_b = 0.5 \text{ m/s}$; $d = 0.001 \text{ m}$; $\sigma = 0.072 \text{ N/m}$ for $Ca = 0.008, 0.03$ and 0.08 ; $\sigma = 0.0072 \text{ N/m}$ for $Ca = 0.5, 0.7$ and 0.8 .

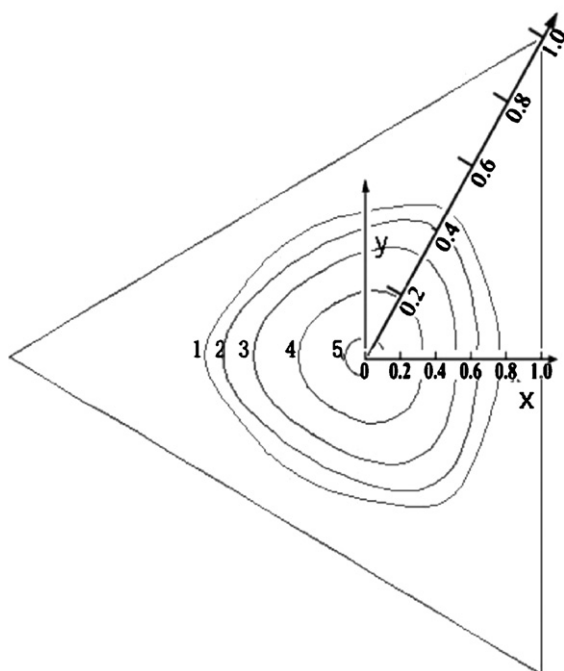


Fig. 12. Toroidal vertexes distribution across a equi-triangular capillary d before the bubble nose: (1) $Ca=0.008$, (2) $Ca=0.05$, (3) $Ca=0.2$, (4) $Ca=0.5$ and (5) $Ca=0.7$; $\rho_L=998.2 \text{ kg/m}^3$; $U_b=0.5 \text{ m/s}$; $d=0.001 \text{ m}$; $\sigma=0.072 \text{ N/m}$ for $Ca=0.008$ and 0.05 ; $\sigma=0.0072 \text{ N/m}$ for $Ca=0.2, 0.5$ and 0.7 .

uid inside moved toward the bubble. And the toroidal vortex would also vanish when the corresponding critical Ca value was reached.

3.4. Relative velocity

Due to the existence of the liquid film, the bubbles in capillaries always moved faster than the liquid slugs, regardless of the capillary geometry. The two-phase relative velocity W was plotted against Ca in Figs. 13 and 14 at $0.003 \leq Ca \leq 1$. It was

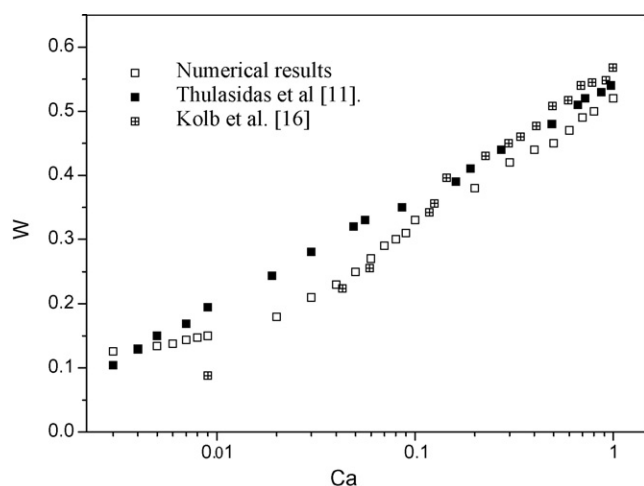


Fig. 13. Two-phase relative velocity, W as a function of Ca in square capillaries. Parameters used in the simulations: $\rho_L=998.2 \text{ kg/m}^3$; $U_b=0.5 \text{ m/s}$; $d=0.001 \text{ m}$; $\sigma=0.072 \text{ N/m}$ for $Ca \leq 0.09$; $\sigma=0.0072 \text{ N/m}$ for $Ca \geq 0.1$.

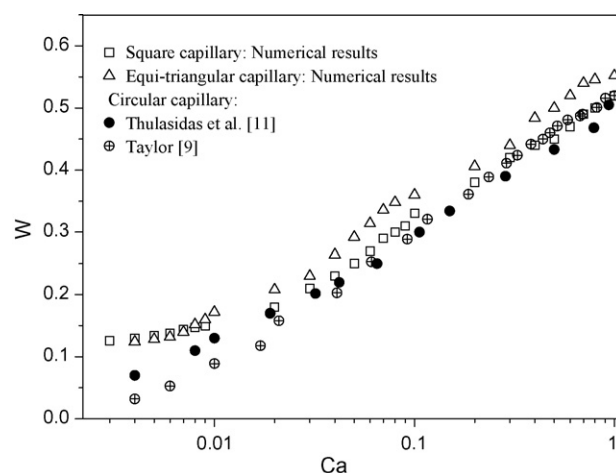


Fig. 14. Two-phase relative velocity, W as a function of Ca in various capillaries. Parameters used in the simulations: $\rho_L=998.2 \text{ kg/m}^3$; $U_b=0.5 \text{ m/s}$; $d=0.001 \text{ m}$; $\sigma=0.072 \text{ N/m}$ for $Ca \leq 0.09$; $\sigma=0.0072 \text{ N/m}$ for $Ca \geq 0.1$.

clear that W increased with increasing Ca in all capillaries. The simulations were consistent with the experimental values measured by Thulasidas et al. [11] and Kolb et al. [16] in square capillaries in Fig. 13.

As discussed in Section 3.1, the flow on diagonal and side planes was remarkably different for the Taylor flow in polygonal capillaries. In order to analyze the influence of capillary geometry on W , the numerical results in square and equi-triangular capillaries were compared with the previous studies in circular capillaries in Fig. 14. W in circular capillaries was smaller than that in square and equi-triangular capillaries at low and intermediate Ca , but overlapped partially with that in square capillaries at high Ca . The closer similarity between circular and square capillaries was responsible for the slight difference in the relative velocities. Fig. 14 showed that the relative velocities in square capillaries were larger than that in equi-triangular capillaries at low Ca . This might be caused by the fact that the area of close contact between bubble and wall was larger in equi-triangular capillaries than that in square capillaries.

4. Conclusions

The VOF method of computational fluid dynamics was used to investigate the hydrodynamic characteristics of Taylor flow in square and equi-triangular capillaries. Different from circular capillaries, Taylor flow in polygonal capillaries was non-circular-symmetric. The flow in the sides of polygonal capillaries was different from that in the corners. The bubble shape, film thickness, velocity field and relative velocity were studied as functions of capillary number. The results agreed favorably with that in the open literatures. The effects of the capillary number on the parameters mentioned above were similar in square, equi-triangular and circular capillaries. The comprehensive understanding of hydrodynamic characteristics will be helpful to reveal how to enhance mass and heat transfer in Taylor flow, and also might optimize the design and operation of gas–liquid–solid monolithic reactors.

Appendix A. Nomenclature

Ca	capillary number = $\mu_L U_b / \sigma$
d	capillary hydraulic diameter (m)
\vec{F}	external body forces (N/m ³)
\vec{g}	acceleration due to gravity (m/s ²)
L_b	length of bubble (originating from bubble nose) (m)
\vec{n}	normal vector to the bubble surface
\hat{n}	unit normal vector
p	pressure (Pa)
R_b	bubble radius (m)
R_{b_AB}	bubble radius in AB direction (m)
R_{b_AC}	bubble radius in AC direction (m)
R_c	capillary hydraulic radius (m)
t	time (s)
U_b	bubble velocity (m/s)
U_L	liquid slug velocity (m/s)
UDF	user defined function
\vec{v}	velocity vector (m/s)
W	relative velocity = $(U_b - U_L) / U_b$

Greek letters

α	volume fraction in a grid cell
α_G	volume fraction of gas phase in a grid cell
α_L	volume fraction of liquid phase in a grid cell
δ	liquid film thickness (m)
μ	molecular viscosity (kg/m s)
μ_L	liquid molecular viscosity (kg/m s)
μ_G	gas molecular viscosity (kg/m s)
θ	degree of angle
κ	free surface curvature
ρ	density (kg/m ³)
ρ_L	liquid density (kg/m ³)
ρ_G	gas density (kg/m ³)
σ	surface tension (N/m)

Subscripts

G	gas phase
L	liquid phase

References

- [1] T. Boger, A.K. Heibel, C.M. Sorensen, Monolithic catalysts for the chemical industry, *Ind. Eng. Chem. Res.* 43 (2004) 4602–4611.
- [2] T.A. Nijhuis, M.T. Kreutzer, A.C.J. Romijn, F. Kapteijn, J.A. Moulijn, Monolithic catalysts as efficient three-phase reactors, *Chem. Eng. Sci.* 56 (2001) 823–829.
- [3] S. Roy, T. Bauer, M. Al-Dahhan, P. Lehner, T. Turek, Monoliths as multi-phase reactors: a review, *AIChE J.* 50 (2004) 2918–2938.
- [4] M.T. Kreutzer, F. Kapteijn, J.A. Moulijn, J.J. Heiszwolf, Multiphase monolith reactors: chemical reaction engineering of segmented flow in microchannels, *Chem. Eng. Sci.* 60 (2005) 5895–5916.
- [5] A. Stankiewicz, Process intensification in in-line monolithic reactor, *Chem. Eng. Sci.* 56 (2001) 359–364.
- [6] L.R. Snyder, H.J. Adler, Dispersion in segmented flow through glass tubing in continuous-flow analysis, *Anal. Chem.* 48 (1976) 1017–1027.
- [7] H. Pedersen, C. Horvath, Axial dispersion in a segmented gas–liquid flow, *Ind. Eng. Chem. Fundam.* 20 (1981) 181–186.
- [8] F. Fairbrother, A.E. Stubbs, Studies in electro-endosmosis. Part VI. The ‘bubble-tube’ method of measurement, *J. Chem. Soc.* 1 (1935) 527–529.
- [9] G.I. Taylor, Deposition of a viscous fluid on the wall of a tube, *J. Fluid Mech.* 10 (1961) 161–165.
- [10] F.P. Bretherton, The motion of long bubbles in tubes, *J. Fluid Mech.* 10 (1961) 166–188.
- [11] T.C. Thulasidas, M.A. Abraham, R.L. Cerro, Bubble-train flow in capillaries of circular and square cross section, *Chem. Eng. Sci.* 50 (1995) 183–199.
- [12] T. Taha, Z.F. Cui, Hydrodynamics of slug flow inside capillaries, *Chem. Eng. Sci.* 59 (2004) 1181–1190.
- [13] S. Irandoust, B. Andersson, Liquid film in Taylor flow through a capillary, *Ind. Eng. Chem. Res.* 28 (1989) 1684–1688.
- [14] P. Aussillous, D. Quere, Quick deposition of a fluid on the wall of a tube, *Phys. Fluids* 12 (2000) 2367–2371.
- [15] T.C. Thulasidas, M.A. Abraham, R.L. Cerro, Flow patterns in liquid slugs during bubble-train flow inside capillaries, *Chem. Eng. Sci.* 52 (1997) 2947–2962.
- [16] W.B. Kolb, R.L. Cerro, Coating the inside of a capillary of square cross section, *Chem. Eng. Sci.* 46 (1991) 2181–2195.
- [17] W.B. Kolb, R.L. Cerro, The motion of long bubbles in tubes of square cross section, *Phys. Fluids A* 5 (1993) 1549–1557.
- [18] W.B. Kolb, R.L. Cerro, Film flow in the space between a circular bubble and a square tube, *J. Colloid Interface Sci.* 159 (1993) 302–311.
- [19] J. Ratulowski, H.C. Chang, Transport of gas bubbles in capillaries, *Phys. Fluids A* 10 (1989) 1642–1655.
- [20] F. Kamisli, Flow of a long bubble in a square capillary, *Chem. Eng. Proc.* 42 (2003) 351–363.
- [21] T. Taha, Z.F. Cui, CFD modeling of slug flow inside square capillaries, *Chem. Eng. Sci.* 61 (2006) 665–675.
- [22] A.L. Hazel, M. Heil, The steady propagation of a semi-infinite bubble into a tube of elliptical or rectangular cross-section, *J. Fluid Mech.* 470 (2002) 91–114.
- [23] T. Griffin, W. Weisenstein, V. Scherer, M. Fowles, Palladium-catalyzed combustion methane: simulated gas turbine combustion at atmospheric pressure, *Combust. Flame* 101 (1995) 81–90.
- [24] G.C. Wilson, M.F. Bardon, J.J. Witton, Experimental and computational investigation of flow in catalytic monolith channels, *ASME* (1992) (paper 92-GT-118).
- [25] G. Groppi, E. Tronconi, Theoretical analysis of mass and heat transfer in monolith catalysts with triangular channels, *Chem. Eng. Sci.* 52 (1997) 3521–3526.
- [26] C.W. Hirt, B.D. Nichols, Volume of fluid (VOF) method for the dynamics of free boundaries, *J. Comp. Phys.* 39 (1981) 201–225.
- [27] Fluent 6.0 User’s Guide, Fluent Inc., Lebanon, NH, 2001.
- [28] A. Tomiyama, A. Sou, H. Minagawa, T. Sakaguchi, Numerical analysis of a single bubble by VOF method, *JSME Int. J. B* 36 (1993) 51–56.
- [29] A. Tomiyama, I. Zun, A. Sou, T. Sakaguchi, Numerical analysis of bubble motion with the VOF method, *Nucl. Eng. Des.* 141 (1993) 69–82.
- [30] J.U. Brackbill, D.B. Kothe, C. Zemach, A continuum method for modeling surface tension, *J. Comp. Phys.* 100 (1992) 335–354.
- [31] D.L. Youngs, Time-dependent multi-material flow with large fluid distortion, in: K.W. Morton, M.J. Baines (Eds.), *Numerical Methods for Fluid Dynamics*, Academic Press, 1982.
- [32] H.L. Goldsmith, S.G. Mason, The flow of suspensions through tubes. II. Single large bubbles, *J. Colloid Interface Sci.* 18 (1963) 237–261.